The International Journal of Advanced Manufacturing Technology
https://doi.org/10.1007/s00170-026-17871-7

ORIGINAL ARTICLE

Understanding spatial variability in mechanical properties of laser powder-bed fusion parts under material uncertainty

Umesh Kizhakkinan[1] · Jakub Mikula[2] · Shemuel Joash Kuehsamy[2] · Yingzhi Zeng[2] · Kewu Bai[2] · Robert Laskowski[2] · Nagarajan Raghavan[3] · Guglielmo Vastola[2] · Yong-Wei Zhang[2]

Received: 18 November 2025 / Accepted: 10 March 2026

Abstract
Industrial production of high-quality components by laser powder-bed fusion (PBF-L) additive manufacturing requires careful assessment of the combined role of part design, material properties, and process parameters in determining the final component's mechanical properties. Various uncertainties arising throughout the PBF-L process affect the quality of the printed components. Therefore, understanding the impact of different uncertainties on part quality is crucial. In this work, we present a multiscale framework for the quantification and propagation of uncertainty across the PBF-L process. Here uncertainty in material property is considered, where thermal conductivity, specific heat, and density are considered random, and the effect of material uncertainty is studied at the scale of the powder and the scale of the part. The variation in material properties in part is modeled as Gaussian random fields, and the spatial variation of mechanical properties of the printed part is quantified. Also, we quantitatively show how uncertainty propagates from the scale of the part to the scale of the powder, and then back to the scale of the part. We demonstrate the framework with the case of two coupon bars, one printed vertically and the other horizontally on the build plate. We show that, because of the larger impact of heat loss through the baseplate, uncertainty is reduced in horizontal bars as compared to vertical bars, where overheating is possible. According to our research, printing parts having the most contact possible with the baseplate can effectively lower part characteristic uncertainties and improve part quality in real-world additive manufacturing applications.

Keywords Laser powder bed fusion · Material uncertainty · Process-structure-property correlations · Uncertainty quantification · Uncertainty propagation · Gaussian process regression

✉ Nagarajan Raghavan
nagarajan@sutd.edu.sg

✉ Guglielmo Vastola
vastolag@a-star.edu.sg

Umesh Kizhakkinan
umesh_kizhakkinan@sutd.edu.sg

Jakub Mikula
Jakub_Mikula@a-star.edu.sg

Shemuel Joash Kuehsamy
Shemuel_Joash@a-star.edu.sg

Yingzhi Zeng
zengyz@a-star.edu.sg

Kewu Bai
baikw@a-star.edu.sg

Robert Laskowski
rolask@a-star.edu.sg

Yong-Wei Zhang
zhangyw@a-star.edu.sg

[1] Digital Manufacturing and Design Center, Singapore University of Technology and Design (SUTD), 8 Somapah Road, 487372 Singapore, Republic of Singapore

[2] Institute of High Performance Computing (IHPC), Agency for Science, Technology and Research (A*STAR), 1 Fusionopolis Way, #16-16 Connexis, 138632 Singapore, Republic of Singapore

[3] Engineering Product Development, Singapore University of Technology and Design (SUTD), 8 Somapah Road, 487372 Singapore, Republic of Singapore

Published online: 21 March 2026

1 Introduction

Laser powder bed fusion (PBF-L) is a popular metal additive manufacturing (AM) process in which a thin layer of powder material is spread on the build plate, and a laser selectively melts the powder particles based on the part geometry. As the build platform is lowered and the subsequent layer of powder is applied after exposure of the previous layer is completed, the process is repeated to print a part layer by layer. PBF-L is a complex multi-physics process that involves interaction between laser and powder particles, rapid melting of powder particles and formation of melt pool, and grain growth during solidification [1].

A key challenge in the PBF-L process is the variability in the quality of the manufactured product. Various sources of uncertainties are involved in different stages of the PBF-L process that affect the quality of the printed component. The process of investigating the effect of uncertainties on the quantities of interests (QoIs) is known as uncertainty quantification (UQ). A good understanding of different sources of uncertainty and their effect on the QoIs is needed for process planning and quality control of the PBF-L process [2, 3]. UQ can be performed experimentally by printing a component and measuring the quantity of interest. Statistical parameters, including mean and standard deviation of the QoI, can be estimated from the experiment data. Since the PBF-L process involves a myriad of different powder characteristics, alloys compositions, machine settings, and part designs, establishing an UQ approach based on experiments is expensive and time-consuming. On the other hand, a computational approach with model-based UQ offers a faster and lower cost route towards extensively assessing UQ in AM builds.

Uncertainty sources in the PBF-L process can be classified into aleatory and epistemic. The parameters that are random in nature are considered as aleatoric uncertainty. For example, material property, powder particle size, laser power, scan speed, boundary conditions, etc. show variation and are inherent in the AM process. The aleatory uncertainty is also referred to as irreducible uncertainty. Epistemic uncertainty is caused by a lack of knowledge, which could be reducible by collecting more information. Epistemic uncertainty can be divided into data uncertainty and model uncertainty. Data uncertainty may arise from insufficient measurement data that may lead to uncertainty in the distribution type and statistical parameters of a design variable. The difference between a model's prediction and experimental value is referred to as model uncertainty. Model uncertainty comes from the modeling assumptions, numerical approximations, and unknown model parameters [4, 5].

The current state of the art in uncertainty quantification in the PBF-L process is summarized in Table 1. Researchers have considered process and material parameters as different sources of uncertainty, and melt pool size, porosity, stress-strain curve, and residual stress as the quantities of interest. Significant work has been carried out in both forward and inverse UQ investigations. Forward UQ represents the

Table 1 Research on uncertainty quantification in the PBF-L process

Sources of uncertainty	Quantity of interest	Year & reference
Laser power, scan speed, absorption coefficient, latent heat, melting temperature, and thermal diffusivity	Melt pool width	2016 [6]
Laser power, scan speed, and laser beam diameter	Melt pool width	2018 [7]
Laser power, scan speed, layer thickness, laser beam radius, density, specific heat, thermal conductivity, absorption coefficient, latent heat of fusion, and emissivity	Melt pool width	2018 [8]
Thermal conductivity, specific heat, density, absorption coefficient, grain boundary energy, and thermal activation energy of grain growth	Stress–strain curve	2019 [9]
Powder absorptivity and extinction coefficient, thermal conductivity of powder, Young's modulus, yield strength, and strain hardening coefficient	Residual thermal stress	2019 [10]
Thermal gradient, solidification velocity, liquid diffusivity, Gibbs–Thomson coefficient, and segregation coefficient	Microstructural microsegregation	2019 [11]
Preheating and ambient temperatures, absorption coefficient, beam diameter, heat convection coefficient at the surface	Porosity	2020 [12]
Density, specific heat, thermal conductivity, latent heat of melting, laser power, laser absorption coefficient and penetration depth, and powder packing density	Melt pool size, solidification time	2021 [13]
Laser power, scan speed, spot size, layer thickness, absorption coefficient, powder packing ratio, density, specific heat, thermal conductivity, solidus temperature, latent heat of fusion, and Marangoni coefficient	Melt pool width	2022 [14]
Density, thermal conductivity, specific heat, absorptivity, and melting temperature	Lack-of-fusion porosity	2022 [15]
Thermal conductivity, specific heat, absorption coefficient	Melt pool size	2023 [16]
Laser absorptivity and powder bed porosity	Melt pool size	2024 [17]
Powder convection coefficient and activation temperature	Residual strain	2024 [18]

study of the propagation of various sources of uncertainty in the PBF-L process and the quantification of uncertainty of the QoI. Conversely, in the inverse UQ, the uncertainty in the input parameter, which is difficult to measure and quantify through experiment, and the model discrepancy is estimated by comparing the model prediction with real-world experimental results.

In the forward UQ analysis, a set of uncertain input parameters is identified and a probability distribution is assumed. The QoIs are estimated by running a computational model of the PBF-L process. To accurately estimate the statistical parameters of the QoIs, a significant number of simulations must be run using the computational model, which is computationally expensive. This high computational burden can be overcome by developing a surrogate model of the computational model. Such surrogate is then employed in Monte Carlo simulations to estimate the variation in the QoIs due to uncertainties in the input parameters [19, 20]. The UQ studies reported in the literature (Table 1) focus mainly on studying the variation in the size of the melt pool due to different sources of uncertainties. To simulate the PBF-L process and predict the melt pool size, researchers have employed a variety of thermal models, including Rosenthal's semi-analytical thermal model [6, 8, 14], Eagar–Tsai [7, 17], finite element [9, 11, 12], finite volume [13, 14], discrete element [10, 15], etc. However, these models considered the powder layer to be a continuous media. Response surface [8, 13, 14], generalized polynomial chaos expansion [7], Gaussian process regression [9–12], etc., were used to develop the surrogate models for the UQ. Nath et al. [15] proposed a multi-fidelity Gaussian process regression model to predict the melt pool size and lack-of-fusion porosity by training the model using data from a low-fidelity computational model (Rosenthal's model) and a discrete element-based high-fidelity computational model.

Modeling uncertainty in estimating the melt pool's width was examined by [8]. Numerical, input parameter, and measured uncertainties were used to depict the modeling uncertainty. The study employed melt pool models that were semi-analytical and FEM-based. It was found that the uncertainty predicted by the semi-analytical-based model was larger compared to that of the FEM-based model, since the FEM model was able to consider additional physical phenomena and resulted in higher prediction accuracy. The contribution of input parameter uncertainty to the modeling uncertainty was substantially higher than the numerical and measurement uncertainties, and the contribution of the numerical uncertainty was negligible. This article illustrates in detail why a high-fidelity model is necessary to reduce the modeling uncertainty caused by the assumptions and simplifications of computational models.

In order to perform the forward UQ, the probability distribution of uncertain input parameters is either assumed or calculated from the measurement data. An inverse UQ can be carried out when measuring the uncertainty in particular input parameters is challenging. At this stage, the surrogate model is modified by applying the Bayesian calibration technique, which compares the surrogate model's prediction with the QoI's experimental data. By reducing the discrepancy between the surrogate model's prediction and the experimental data, the Bayesian method forecasts the probability distribution of unknown parameters. Chiappetta et al. [18] performed the inverse UQ on the National Institute of Standards and Technology (NIST)-provided displacement experiment data in order to estimate the probability distribution of the powder convection coefficient and the activation temperature. The forward UQ was subsequently performed using the distribution of both of these parameters in order to forecast the residual strain's uncertainty.

To use PBF-L printed parts for mission-critical applications, it is crucial to be able to assess their reliability by quantifying variations in local mechanical properties caused by uncertainties in the printing process. These uncertainties can arise at multiple stages throughout the process. During the design and optimization of a mission-critical component, accurate prediction of spatial variation in mechanical properties is essential, as the local mechanical property at a specific point depends on the thermal history at that location. For instance, the thermal history is influenced by part geometry and uncertainty in material properties, which leads to spatial variations in local mechanical properties across the part. Therefore, it is important to study the propagation of uncertainty in the PBF-L process to predict the reliability of the printed part.

The body of knowledge listed in Table 1 illustrates a comprehensive understanding of uncertainty quantification of the melt pool size. The quantification of mechanical property uncertainty hasn't received as much attention in the literature. Wang et al. [9] developed a UQ framework to study the uncertainty propagation from process parameters to microstructure, then to mechanical properties of selective electron beam melting (SEBM) AM process. In this work, the sources of uncertainty were parameters that control grain growth (listed in Table 1) while the quantity of interest was the stress-strain curve along the build direction. A finite-element-based heat transfer model was used to simulate a single-track SEBM process and predicted the steady-state temperature field. The temperature field was then provided as the input for a phase-field model to simulate the grain growth. The microstructure from the phase-field model was used for homogenization to predict the stress-strain curve along the build direction. A fast Fourier transform

(FFT)-based crystal elasto-viscoplasticity model was used for homogenization. Various surrogate models based on singular value decomposition (SVD)-Kriging were developed at different levels to perform the uncertainty propagation from process to property.

The grain growth and mechanical property at a point are influenced by the temperature field around that point and the temperature field depends on the part geometry. A part is printed on a base plate and the heat generated during the printing dissipates to the base plate, surrounding powder, and shielding gas. The temperature field inside the part depends on how fast the heat dissipates, which in turn is primarily affected by the part geometry since the majority of the heat dissipation occurs by conduction to the base plate. In the UQ study by [9], a single-track thermal simulation was performed to estimate the temperature field, while the influence of part geometry on the temperature field was not considered. The computational models used in the UQ studies listed in Table 1 treated the powder layer as a continuous medium. To accurately study the mechanical properties of PBF-L printed parts, a high-fidelity multiphysics model capturing powder-scale details, melt pool fluid dynamics, solidification, and grain growth is essential. We use the PBF-L process to print parts with different geometry and for every part geometry, the temperature field during printing is different which results in spatial variation in mechanical property. That means the distribution of mechanical property depends on part geometry and the inherent uncertainty in the PBF-L process. The effect of part geometry and uncertainty on mechanical properties is not addressed in the literature.

In this work, we quantitatively address the combined role of material uncertainty as well as part geometry in affecting yield strength, determining its spatial variations across the component, thus providing a direct route to digitally assess printing quality. Our approach is to establish a UQ framework on the basis of an integrated multiscale representation of the 3D printed component (model-based digital twin), which we discuss in Section 2. A cylindrical bar was considered as the part geometry and the AM process assessment was performed for part alignment along the horizontal and vertical (build) directions. Three material parameters, namely thermal conductivity, specific heat, and density were considered as the sources of uncertainty in the PBF-L process, chosen for their key role in governing heat transfer, and thus microstructure evolution and mechanical properties. While many other sources of uncertainty exist in L-PBF, such as the role of defects [21, 22], in this work, we chose to study the role of material properties, such as thermal properties, which are not significantly influenced by the manufacturing process. These three parameters were modeled as Gaussian random variables and uncertainty in yield strength was quantified. The paper is organized as follows. The multiscale integrated physics-based model used to generate the data is described in Section 2, including the model deployed at the scale of the powder (Section 2.1) and at the scale of the part (Section 2.2). The presentation of our uncertainty quantification and propagation is then discussed in Section 3, specifically, in terms of quantification at the scale of the part (Section 3.1) and of the powder (Section 3.2). Propagation of uncertainty from material to yield strength is discussed in Section 3.3, followed by conclusions.

2 Multiscale modeling of the laser powder-bed fusion process

To perform uncertainty quantification in additive manufacturing processes and assess the reliability of printed parts, experimental investigations are often costly. Numerical simulations provide a cost-effective alternative for investigating variations in process parameters and material properties. A wide range of numerical methods has been developed in the literature to model additive manufacturing processes [23–25]. A multiscale integrated model-based digital twin of the PBF-L process was used to simulate the printing process [26] and provide the data for our UQ framework. The architecture of the digital twin consists of multiple solvers, each one tailored at a specific length scale, integrated together whereby the outputs of one model represent the inputs of the next logical model, in the end-to-end workflow that leads from the global inputs to outputs. The overall workflow for data generation is depicted in Fig. 1. Each simulation begins with choosing a part geometry (STL file), and defining the

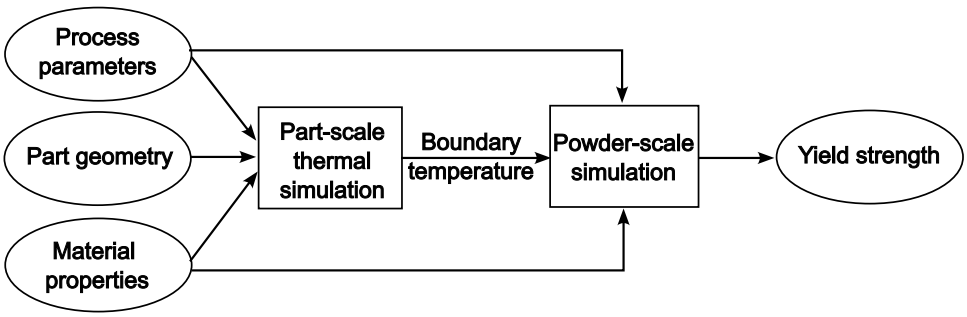

Fig. 1 Workflow of the laser powder bed fusion process simulation

Table 2 Process parameters used for simulation

Parameter	Value
Laser power	285 W
Scan speed	960 mm/s
Layer thickness	40 μm
Hatch spacing	110 μm
Stripe width	10 mm
Recoater time	18 s
Hatch rotation	
Initial orientation	0 degrees
Incremental angle	67 degrees
Scan pass per layer	1
Powder size distribution	
d10	21.37 μm
d50	31.24 μm
d90	49.52 μm

process parameters as well as material properties, as detailed in Tables 2 and 3, respectively. The first step is a finite element thermal simulation at the scale of the part to determine the thermal history for the whole component. From this thermal history, the temperature of each mesh layer at the end of the printing and recoating step is calculated. This temperature is then applied, in a multi-scale fashion, as the boundary condition to a high-fidelity simulation at the scale of the powder which resolves the details of powder particles, melt pool flow, solidification, and grain nucleation and growth [27, 28]. The three-dimensional digital microstructure is then connected as input to a self-consistent mean field homogenization scheme [29] which computes the yield strength of the material.

Table 3 Material properties of the IN718 used for simulation [30]

Parameter	Value
Melting temperature	1553 K
Boiling temperature	3174 K
Density of solid	8440 kg/m^3
Density of liquid	8440 kg/m^3
Specific heat of solid	440 J/kgK
Specific heat of liquid	440 J/kgK
Specific heat of vapour	440 J/kgK
Latent heat of fusion	0.2819×10^6 J/kg
Latent heat of vaporization	5.49×10^6 J/kg
Thermal conductivity of solid	26 W/mK
Thermal conductivity of liquid	26 W/mK
Viscosity of liquid	7.5×10^{-3} Pa.s
Surface tension	1.7 N/m
Marangoni force coefficient	-2.8147×10^{-4} N/mK
Recoil pressure	5.371×10^4 Pa

2.1 Powder-scale simulation

The simulations at powder scale adopt multiphysics approach, where thermal solver, grain growth, solidification, and melt pool fluid dynamic solvers are executed concurrently. The solidification and grain grow solver implements multi phase field approach proposed by [31–33]. The anisotropic grain growth is modeled by introducing orientation dependent solid-liquid interfacial energy [34, 35]. The melt pool flow solver is implemented within incompressible formulation of Lattice Boltzmann Method (LBM). The thermal solver captures the effect of the laser heat source adopting Gaussian shape with 4σ equal to a typical laser beam width of 100 μm. The periodic boundary conditions are set in directions parallel to the substrate, in the perpendicular direction at the bottom face of the Representative Volume Element (RVE), the temperature field is set to a constant value T_B, which is considered as an input parameter. The simulation is executed in layer by layer fashion. The first layer starts with a flat base plate with predefined grain structure generated by Voronoi tesselation of random points seeded inside the plate. At the top of the plate a layer of powder with defined depth and diameter distribution specified by values of d10, d50 and d90 parameters is distributed using simple "rain drop method". Subsequently, the layer undergoes melting under laser heat source in line by line fashion, where the hatch spacing is considered an input parameter. At the end of each line the system is allowed to cool down and solidify completely. The temperature is reset to T_B at the beginning of each line. The subsequent layers repeat this procedure, however the powder is distributed on top of the solidified previous layer. After completing each layer the substrate grows by certain amount (volume of deposited powder). In order to avoid the artifacts related to monotonic increment of substrate thickness this exact amount is cut from the bottom of RVE. After completion of desired number of layers the whole RVE is resembled. The described procedure is depicted in Fig. 2. The details of our simulation model are described in Ref. [28].

The powder-scale simulation was performed on a domain of 500 $\mu m \times 500$ μm with a grid spacing of 5 μm, as shown in Fig. 2a, for ten powder layers, representing a cubic Representative Volume Element (RVE) of printed material. The process parameters used in the simulation are listed in Table 2. The boundary temperature T_B applied as the thermal boundary condition at the lower face of the RVE is the central quantity connecting the powder scale RVE to the part scale. The details of estimating the value of T_B are discussed in Section 2.2. Figure 2b and c illustrate the domain and microstructure after printing ten layers, respectively.

Considering the simulation model, the grain nucleation and growth process are determined by two factors: the cooling

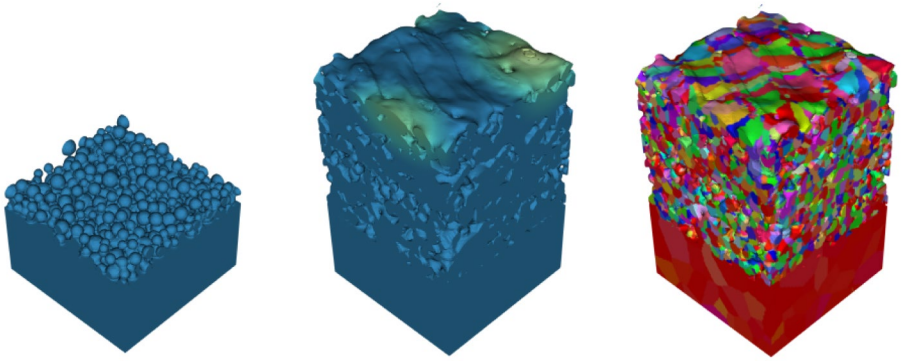

(a) Base plate with powder (b) After printing (c) Microstructure

Fig. 2 Different stages of the powder-scale simulation (**a** and **b**) and (**c**) the grain distribution

rate and the velocity of the solidification front. Those two are not completely independent; during solidification, latent heat is released, which flattens the temperature distribution across the interface, lowering the driving force for solidification. In this scenario, the solidification front is slower than cooling rate a conditions for melt pool under-cooling may arise creating a convenient conditions for nucleation. For performance reasons, in our grain growth model we use a simplified nucleation model [36, 37] where the nucleation flux is controlled by the under-cooling temperature ΔT_N and its standard deviation ΔT_σ (see [28] for implementation details). The cooling rate is mainly governed by the boundary temperature [38], whereas the solidification front velocity is controlled by the interfacial mobility. In the scope of this work the interfacial mobilities and nucleation model parameters are kept fixed (see Table 3), while the effect of the boundary temperature is discussed. In particular, the mobilities of the solid-solid (grain), solid-vapor, and liquid-vapor interface were temperature-independent, while a simple linear relationship was implemented for the dependence of the solid-liquid interface mobility on temperature [39]. The set of parameters allow in some extent to control and design grain microstructure. In fact, at given process parameters (energy density), a low boundary temperature results in higher cooling rates and therefore a higher driving force for grain nucleation, but more importantly higher chance for under-cooling. This results in statistically smaller grain size comparing to the effects of applying higher boundary temperature.

To quantitatively analyze the effect of boundary temperature on the cooling rate, a series of powder-scale simulations were conducted for boundary temperature values ranging from 300 K to 1200 K. In this case, a single-track simulation was performed on a domain of 2000 μm × 500 μm for one layer. The thermal history at the center of the layer was extracted and is presented in Fig. 3a for different values of boundary temperatures. As depicted in Fig. 3, the boundary temperature directly affects the thermal history at a specific point and the resulting cooling rate. The cooling rate was estimated from the thermal history data between the liquidus and solidus temperatures. The average cooling rates corresponding to different boundary temperatures are illustrated in Fig. 3b. The results indicate that a lower boundary temperature leads to a higher cooling rate, while an increase in boundary temperature results in a reduction of the cooling rate.

From the microstructure shown in Fig. 2c, a subdomain of size 460 μm × 460 μm × 400 μm was extracted to

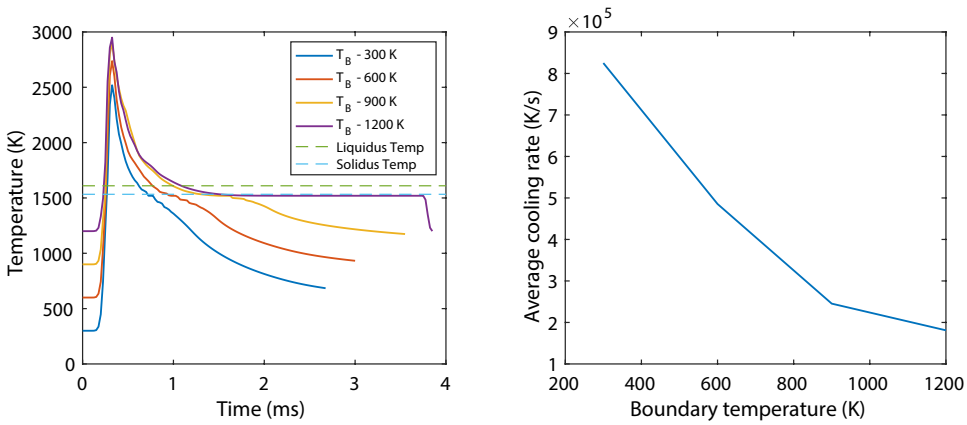

(a) (b)

Fig. 3 Effect of boundary temperature on (**a**) thermal history and (**b**) cooling rate

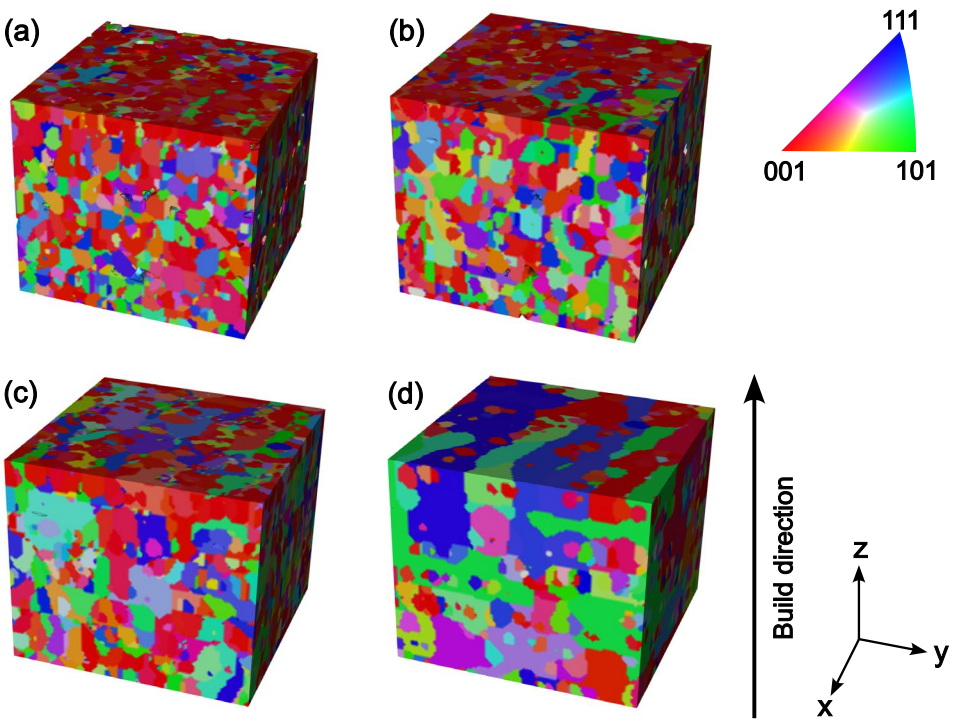

Fig. 4 A subdomain of size 460 $\mu m \times$ 460 $\mu m \times$ 400 μm extracted from Fig. 2c for different values of boundary temperatures: (**a**) 300 K (**b**) 600 K (**c**) 900 K (**d**) 1200 K. The grain size increased with an increase in the boundary temperature

remove grain growth boundary effects from the RVE. Figure 4 represents the microstructure of the subdomain from the powder-scale simulations performed for different values of boundary temperatures. Grain morphology is influenced by the cooling rate; finer grains are produced at a higher cooling rate [38]. Since the cooling rate is higher at a lower value of boundary temperature, such conditions resulted in finer grains for the boundary temperature value of 300 K, as shown in Fig. 4a. In the case of 1200 K boundary temperature, coarser grains can be observed in Fig. 4d due to the lower value of cooling rate. The grain data was extracted from the subdomain and shown in Fig. 5. The grain area across the $x - z$ plane was extracted and the histogram of grain area for boundary temperatures of 300 K and 1200 K is displayed in Fig. 5a. It is evident that over half of the grains have an area of less than 100 μm^2 at the 300 K boundary temperature. This indicates that finer grains predominate in the microstructure. The grain volume data was extracted from the subdomain, and the average grain volume for different values of boundary temperature is shown in Fig. 5b. Average grain volume increases with an increase in boundary temperature.

Polycrystal homogenization based on a mean field self-consistent scheme [40] was performed on the subdomain shown in Fig. 4. Figure 6a displays the stress-strain curves for different boundary temperatures along the x and z directions. The yield strength estimated from the stress-strain curve is shown in Fig. 6b. It can be seen that there is a reduction in yield strength with an increase in boundary temperature. Because a higher boundary temperature leads

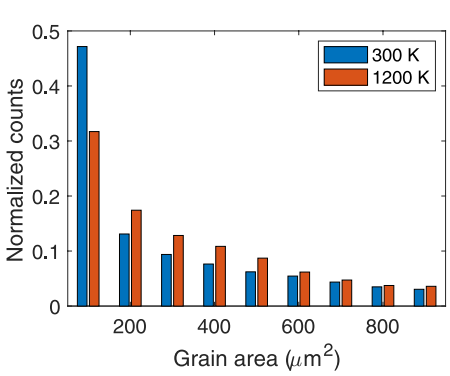

(a)

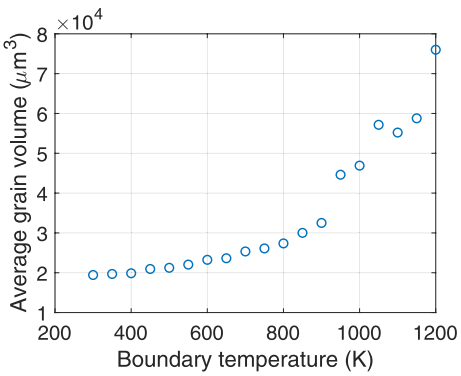

(b)

Fig. 5 Effect of boundary temperature on grain size (**a**) histogram of grain area in the $x - z$ plane (**b**) relationship between the boundary temperature and the average grain volume

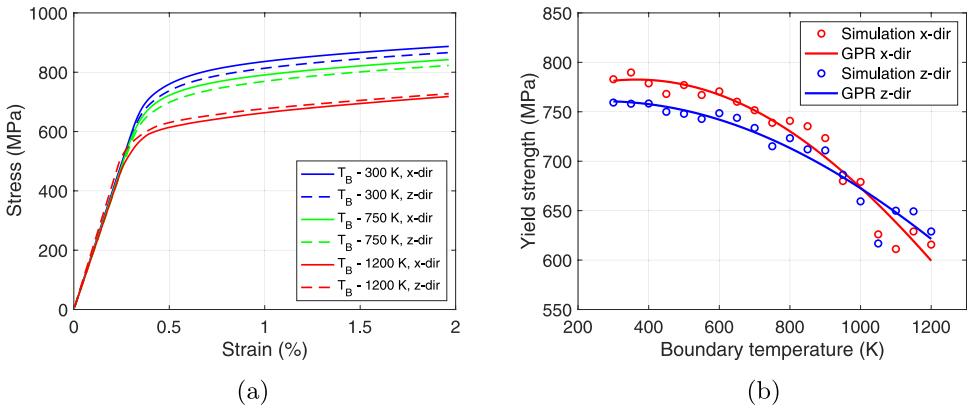

Fig. 6 (**a**) Stress–strain curves generated from polycrystal homogenization in $x-$ and $z-$ directions for different boundary temperatures (T_B). (**b**) The effect of boundary temperature on yield strength. The yield strength was estimated from the stress-strain curves in $x-$ and $z-$ directions. The Gaussian process regression (GPR) method was used to fit the simulation data

to a slower cooling rate, resulting in coarser grains [38]. It can also be seen that an anisotropy exists at lower boundary temperatures because the majority of grains are oriented along the build direction ([001]) which can be visible in Fig. 4a. The phenomenon of anisotropy is less significant at higher boundary temperature because the grains are oriented in all directions, as shown in Fig. 4d. The simulation data shown in Fig. 6b were used to train two Gaussian process regression (GPR) models [41] in the *x* and *z* directions, with the input being boundary temperature and the output being yield strength. As the boundary temperature has the role of far-field temperature relative to the top region of the powder-scale model, which is at or near the melting temperature (1553 K), our GPR model was trained to up to 1200 K. The yield strength predicted by the GPR models for the boundary temperature ranging from 300 K to 1200 K is shown by the solid line in Fig. 6b.

2.2 Part-scale thermal simulation

The part-scale thermal simulation was based in finite elements. The methodology adopted in this work follows planar heating simulations, such as [42] where multiple real powder layers are lumped together into one finite element layer. For computational efficiency, no moving heat source was considered, while an average heat rate was applied to the whole finite element layer. The heat equation was solved using a fully implicit scheme, remaining stable for large time steps. Temperature contours were predicted at every finite element layer and the thermal history was extracted for every node of the finite element mesh.

A cylindrical bar with 7 mm diameter and 40 mm height was considered in this study. The part-scale thermal simulations of the bar were performed in horizontal and vertical build directions, as shown in Fig. 7. A base plate of size

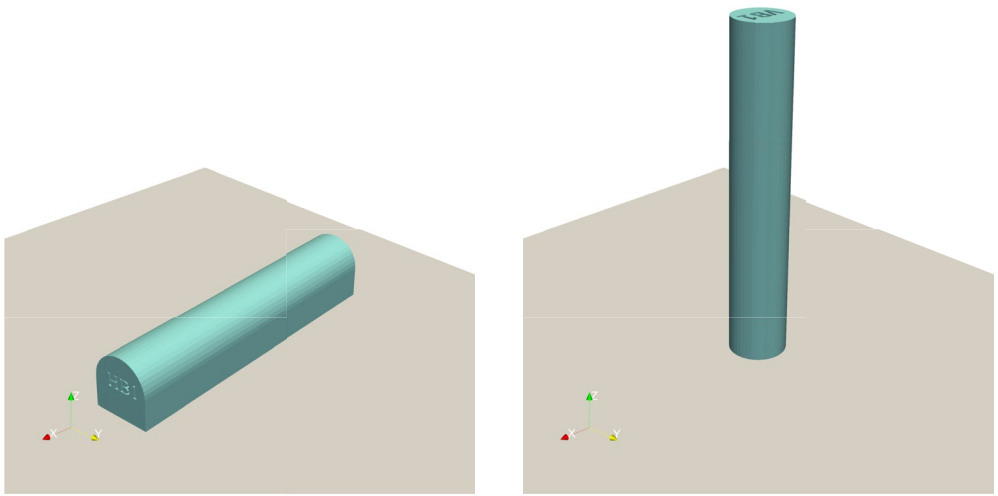

Fig. 7 Geometric representation of the bars printed (**a**) horizontally and (**b**) vertically

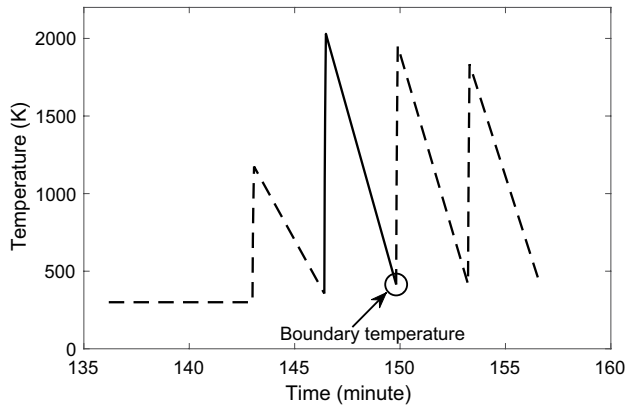

Fig. 8 Thermal history of an element at n^{th} element layer. Temperature value of an element was estimated by taking the average of nodal temperatures. The solid line represents the thermal history during the printing of n^{th} element layer and the dashed line represents the heat conducted while printing the adjacent layers

74.3 mm × 90.6 mm × 9.58 mm was used for the simulation. Inclusion of the baseplate was crucial to obtain accurate thermal fields at part scale, allowing for heat to be dissipated away from the part through conduction into the baseplate. The mesh was generated with a voxel size of 0.5 mm with 8-node brick elements. A thermal boundary condition of 300 K was applied at the bottom of the base plate and an initial temperature of 300 K for each mesh layer was also applied. Ambient temperature was kept at 300 K and a natural convective heat transfer from the top surface was considered with the coefficient h = 20 W/(m^{2}K).

The finite element solution provided the thermal history of the nodes and the thermal history at the center of the element was estimated by taking the average of nodal thermal histories. The thermal history at the center of an element for the n^{th} element layer is shown in Fig. 8. The solid line represents the thermal history during the printing of the n^{th} element layer. The steady-state temperature of the n^{th} element layer after printing was defined as the boundary temperature and marked in a circle in Fig. 8. The value of the boundary temperature from the part-scale thermal simulation was applied as the thermal boundary condition in the powder-scale model to estimate mechanical properties. The details of the powder-scale simulation are given in Section 2.1. The dashed line in Fig. 8 represents the heat conducted while printing the adjacent layers, which was not used to estimate the boundary temperature.

Part-scale thermal simulations were carried out for the bars oriented horizontally and vertically and the boundary temperature value for every element was estimated. The boundary temperature distribution of horizontal and vertical bars are shown in Fig. 9a and b, respectively. The heat generated during the printing of the horizontal bar easily conducts to the base plate due to the large contact area between the part and the base plate. So, the boundary temperature for the horizontal bar is lower. However, the contact area between the vertical bar and the base plate is low and the heat accumulated during the printing does not conduct easily to the build plate. Such conditions resulted in a higher value of boundary temperature for the vertical bar as compared to the horizontal bar.

From the boundary temperature distribution displayed in Fig. 9, the yield strength distribution for each bar was predicted using the machine learning model referenced in Fig. 6b, and is displayed in Fig. 10. Here, yield strength along the *x* direction is plotted for the horizontal bar (in Fig. 10a) and yield strength along the *z* direction for the vertical bar (in Fig. 10b) based on the loading directions while conducting the tensile tests. It can be seen from Fig. 10 that the horizontally built bar has a higher value of yield strength and it is homogeneous through the part. On the other hand, the vertically built bar shows a slightly lower value of yield

Fig. 9 Boundary temperature distribution in the (**a**) horizontal and (**b**) vertical bars from part-scale thermal simulation

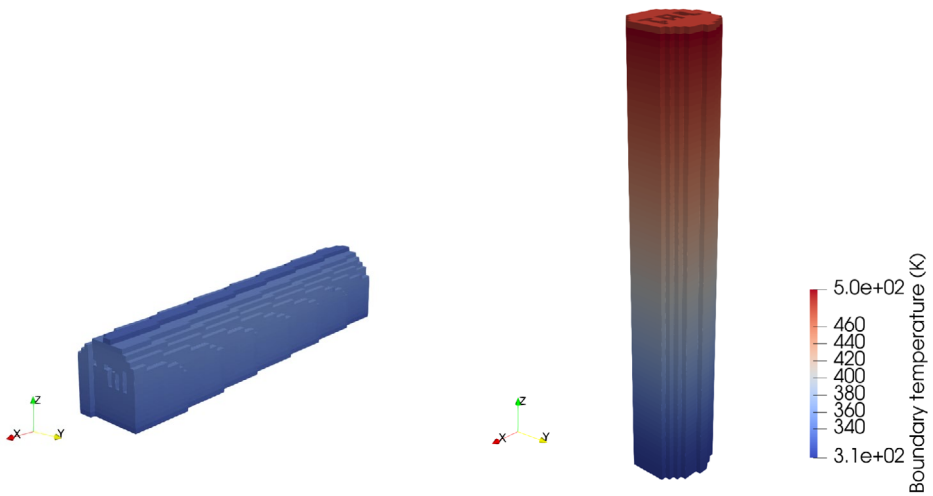

(a) Horizontal (b) Vertical

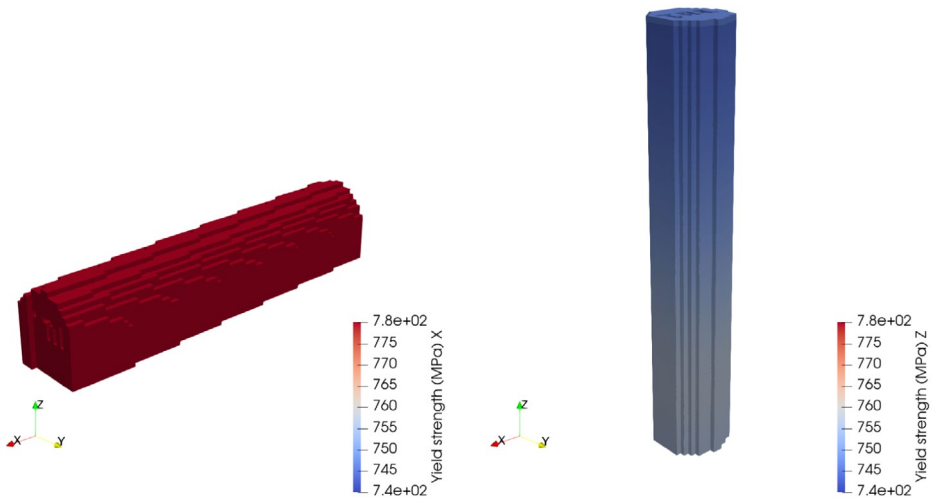

(a) Horizontal (b) Vertical

Fig. 10 Yield strength distribution in the (**a**) horizontal and (**b**) vertical bars. Using the GPR model (Fig. 6b) and the boundary temperature distribution from the part-scale thermal simulation (Fig. 9), the yield strength was computed

strength and reduces with an increase in the build height. It can be concluded that when a part is printed vertically, the part temperature increases and that affects the microstructure, ultimately resulting in a lower and inhomogeneous distribution of yield strength. Hence, parts should be printed in as close contact as possible with the baseplate to ensure higher strength and a homogeneous distribution of mechanical properties.

3 Uncertainty quantification and propagation

Material uncertainty was considered for uncertainty quantification and propagation in the PBF-L process. Among the material parameters listed in Table 3, thermal conductivity, specific heat, and density were considered random variables. A ±15% variation in each random variable was assumed and it follows a Gaussian distribution. To quantify the uncertainty in the quantity of interest, simulations using a high-fidelity model must be carried out for the random samples of the input parameters. This approach is popularly known as Monte Carlo simulation (MCS). However, running MCS using the high-fidelity model is computationally expensive. To overcome this issue, a machine-learning model was developed using the Gaussian Process Regression (GPR) method at different scales. A stratified sampling technique, Latin hypercube sampling (LHS), was used to generate the random samples of input variables. In the case of a simple random sampling technique, a large amount of random samples are required to represent the entire population. However, in the LHS approach, the probability distribution is divided into equally-probable non-overlapping intervals, and a sample is randomly selected from each interval. This approach requires less number of random samples to represent the distribution. Part- and powder-scale simulations were carried out for the LHS random samples for uncertainty quantification. This section discusses the impact of material uncertainty at the scales of the powder and of the part.

3.1 Uncertainty quantification at part-scale

The impact of material uncertainty on the boundary temperature is discussed in this section. Thermal conductivity, specific heat, and density were considered as random variables. LHS random samples of size 30×3 were generated and the part-scale thermal simulations were performed for horizontal and vertical bars. The boundary temperature along the center of the vertical bar is shown in Fig. 11 for the 30 random samples. It can be seen that material uncertainty results in variability in the boundary temperature.

As a representative location inside for each component, the boundary temperature of the element at the center of the horizontal and vertical bars was extracted and used to train two GPR models for horizontal and vertical cases. In these GPR models, thermal conductivity, specific heat, and density were the input while the boundary temperature was the output. MCS was performed using the GPR models and the distribution of the boundary temperature is shown in Fig. 12. The mean and standard deviation of boundary temperature for the horizontal bar in Fig. 12a are 323.92 K and 2.50 K, respectively, and for the vertical bar in Fig. 12b are 415.42 K and 10.65 K, respectively. The percentage of the coefficient of variation (standard deviation/mean) for horizontal and vertical bars are 0.77% and 2.56%, respectively, and it is clear that the effect of material uncertainty is significantly higher in the vertically-built bar.

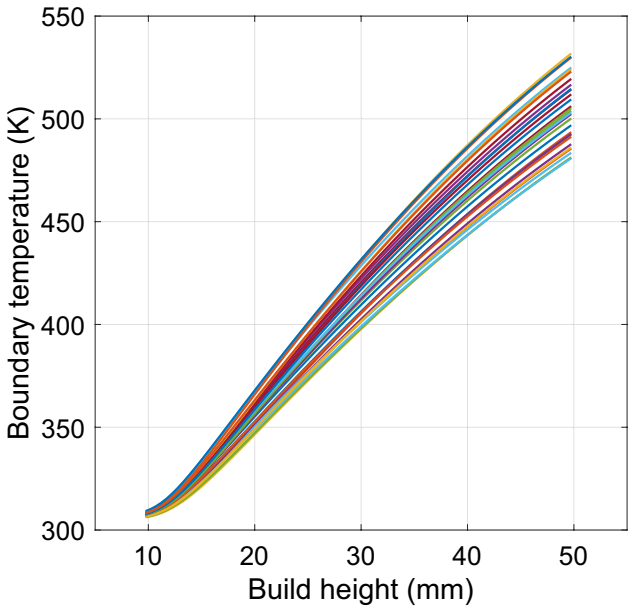

Fig. 11 Effect of material uncertainty on the boundary temperature distribution of the vertical bar. The boundary temperature values were extracted along the center of the bar

3.2 Uncertainty quantification at Powder-scale

An LHS sample of size 430 × 4 was generated for thermal conductivity, specific heat, density, and boundary temperature. The yield strength was determined by running the powder-scale model based on the LHS samples. The GPR model for the powder scale was trained using this data. The yield strength distribution is displayed in Fig. 13. Due to material uncertainty, variations in the yield strength can be observed for a specific value of boundary temperature and the variation is larger at higher boundary temperature. Two GPR models were trained for x and z directions and MCS was performed using the GPR model to quantify the effect of material uncertainty on the yield strength. A Gaussian random sample size of 10000 × 3 was generated for thermal conductivity, specific heat, and density. MCS was performed using the random sample for different values of boundary temperature ranging from 300 K to 1200 K, and mean and standard deviation of the yield strength was estimated for various values of boundary temperature. The solid line in Fig. 13a and b indicates the predicted mean value and the dashed-dotted line depicts the confidence interval. Figure 6b represents the deterministic case without considering the material uncertainty. Due to material uncertainty, variation in the value of yield strength can be observed for a specific value of boundary temperature and it is represented as the confidence interval in Fig. 13. A significant variation in yield strength can be seen at higher boundary temperature.

3.3 Uncertainty propagation

The objective of uncertainty propagation analysis is to understand how different sources of uncertainty influence the outcome of a process and impact the target variable–in this case, the yield strength distribution of a part fabricated using the PBF-L process. In this study, variations in thermal conductivity, specific heat, and density were identified as primary sources of uncertainty, as their precise experimental measure is influenced by numerous factor that alter their value, including the exact alloy composition, instrumentation, and methodology of measure [30, 43]. The thermal history at any given point is determined by process parameters, material properties, and part geometry, which plays a crucial role in grain growth and thus in determining the mechanical properties of the part. In this work, process parameters were held constant while uncertainties in material properties were the focal point. These uncertainties propagate through the various stages of the PBF-L process, leading to yield strength variability for specific part geometries. Since uncertainty propagation differs with geometry, a bar geometry was selected for this study to examine the effects of build orientation on uncertainty propagation.

Fig. 12 Boundary temperature distribution at the center of the bar due to material uncertainty

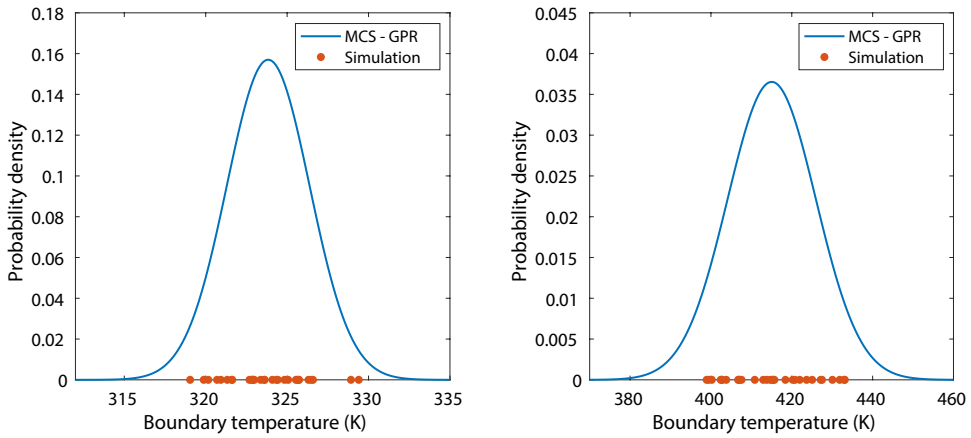

(a) Horizontal (b) Vertical

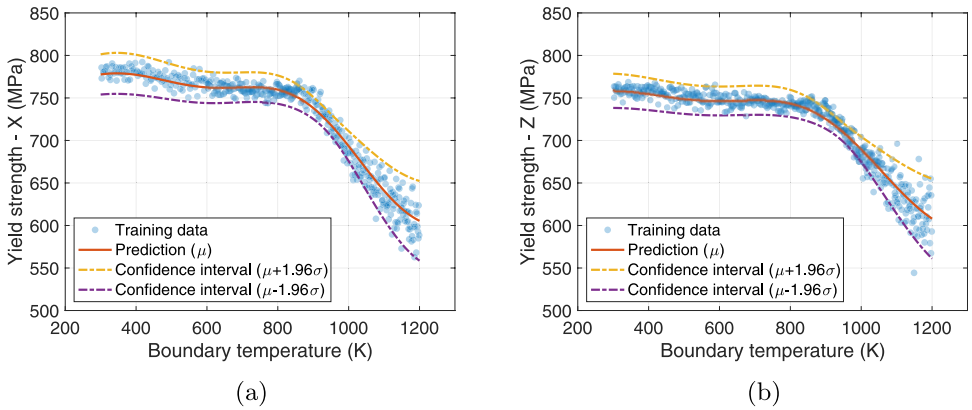

Fig. 13 Uncertainty quantification of yield strength. Here, thermal conductivity, specific heat, and density were considered as the uncertainty source

Our uncertainty propagation flow chart for the PBF-L process is shown in Fig. 14. The PBF-L process is a multi-physics and multi-scale process. We have two process models at part and powder scales. First, the material parameters (thermal conductivity, specific heat, and density) were modeled as Gaussian random variables, and the variation in boundary temperature was estimated by running multiple part-scale thermal simulations, which is discussed in Section 3.1. Then the yield strength was calculated using the powder-scale GPR surrogate model discussed in Section 3.2. The parameters considered here were modeled as a spatially correlated random field for uncertainty propagation to represent natural variability. The matrix decomposition approach [44, 45] was used to create Gaussian random fields of thermal conductivity, specific heat, density, and boundary temperature. An exponential covariance function with a correlation length of 15 mm was used in the matrix decomposition method. Such value of correlation length was chosen to ensure smooth random fields across part geometry, consistently with the smoothness of the mechanical fields it intends to model. These random fields were input into the powder-scale GPR model to determine the spatial variation of the yield strength in the part.

Figure 15 illustrates the spatial variation in yield strength for horizontal and vertical built bars due to material uncertainty. For the horizontal bar, yield strength along the x-direction is shown in Fig. 15a, while for the vertical bar, yield strength along the z-direction is presented in Fig. 15b, in alignment with the loading directions used during tensile testing. Figure 15c provides a comparative distribution of yield strength for both orientations. The observed variation in yield strength arises from two main factors. The first factor is the build orientation, as discussed in Section 2.2, where part orientation on the build plate influences thermal history, leading to differences in yield strength. The second contributing factor is material uncertainty. The combined impact of these factors results in significant yield strength variation, as evident in Fig. 15c, where the horizontally built bar demonstrates a higher yield strength than the vertically built one.

The procedure described in the preceding paragraph needs to be repeated for a large number of input random fields to quantify the uncertainty of the yield strength. For this reason, 1000 random field samples were generated and the yield strength distribution was predicted for both horizontal and vertical bars. Data in the center of the bar was extracted to display the propagation of uncertainty. The distribution of

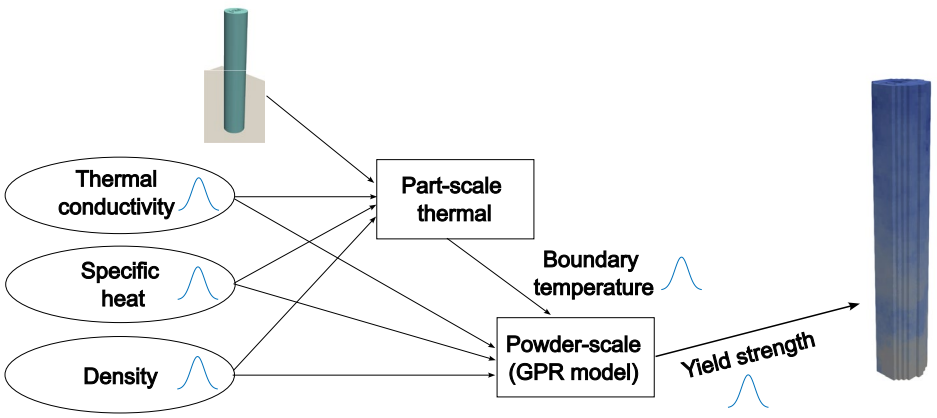

Fig. 14 Uncertainty propagation flow-chart

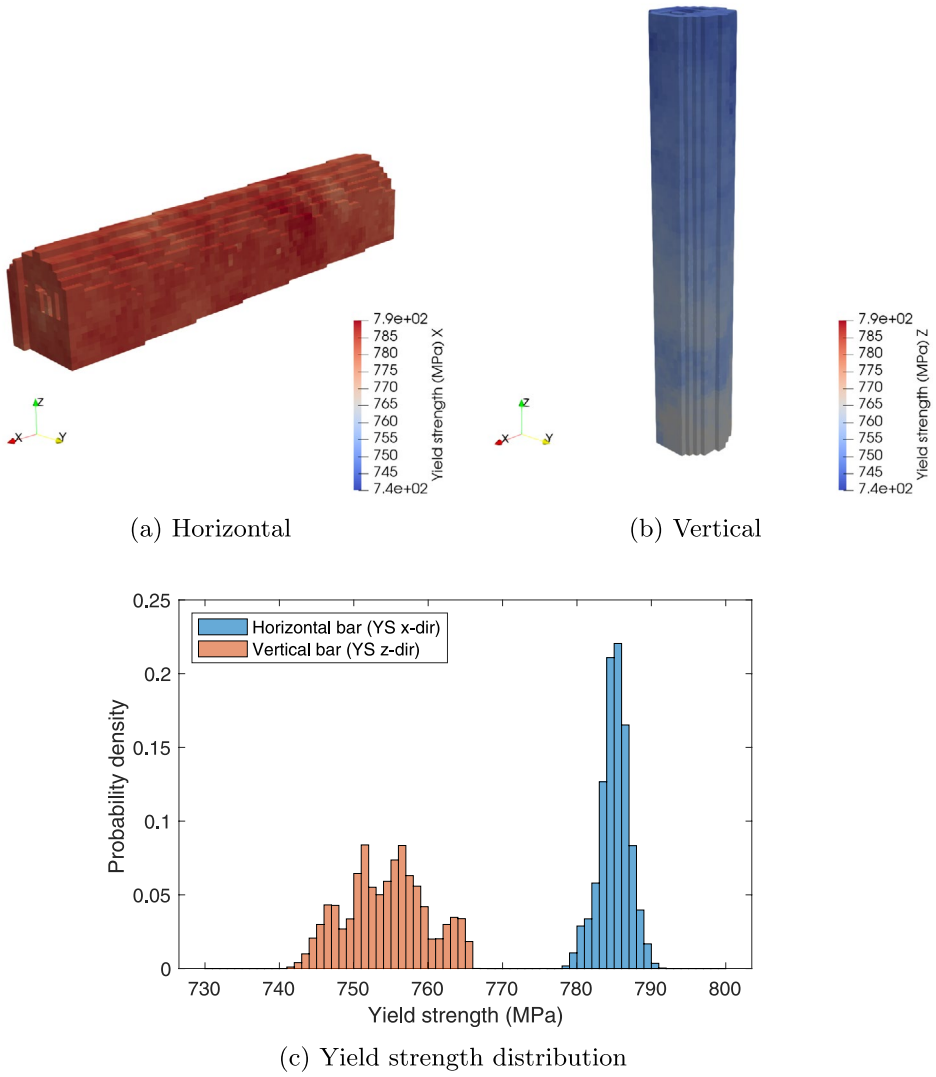

(a) Horizontal (b) Vertical

(c) Yield strength distribution

Fig. 15 Yield strength distribution in the horizontal and vertical bars

thermal conductivity, specific heat, and density are shown in Fig. 16a, b, and c, respectively. The coefficient of variation of the distributions is 5%. The uncertainty in material properties propagates through the part-scale thermal model and results in variation in the boundary temperature. The distribution of the boundary temperature in the center of the vertical bar is shown in Fig. 16d. The coefficient of variation of the boundary temperature is 2.56%.

The distribution of the yield strength in the center of the horizontal and vertical bars due to uncertainty in material properties is shown in Fig. 17. The coefficients of variation for the horizontal and vertical bars are 0.3992% and 0.3846%, respectively. The distribution of the coefficient of variation (%) in the horizontal and vertical bars is shown in Fig. 18. The values of coefficient of variation vary between 0.32 and 0.55.

This study demonstrates how part orientation and inherent material uncertainties contribute to spatial variations in the mechanical properties of parts fabricated via the laser powder bed fusion (PBF-L) process. For vertically built bars, heat accumulation during printing significantly influences yield strength. In this study, fixed process parameters were used to simulate the PBF-L process. However, heat accumulation could be minimized with adaptive processing, where laser power and scan speed are adjusted based on surface temperature. Real-time temperature data processing would enable the optimization of process parameters to reduce yield strength variation. The approach detailed in this paper could be integrated into optimization algorithms to improve yield strength predictions.

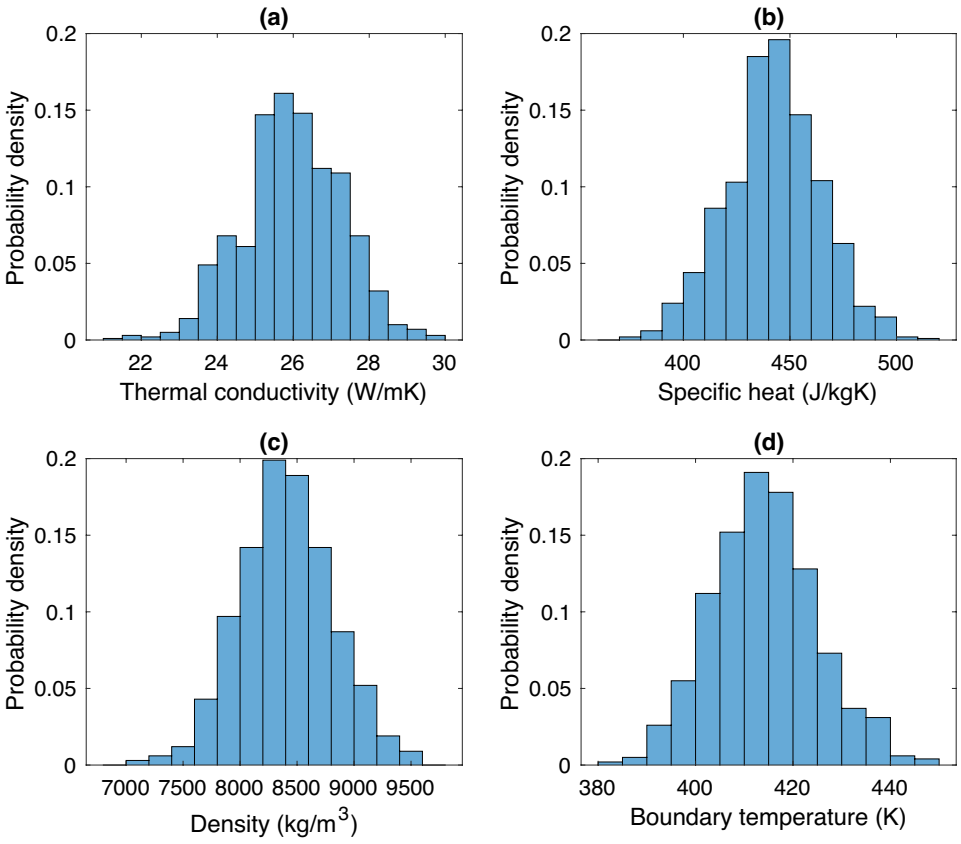

Fig. 16 Uncertainty in the input material parameters (**a**), (**b**), (**c**), and (**d**) distribution of boundary temperature in the center of the vertical bar due to uncertainty in material properties

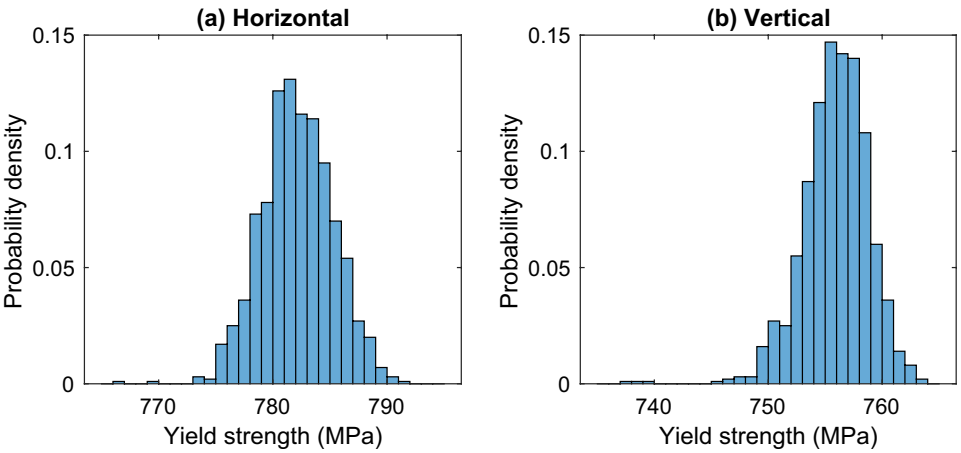

Fig. 17 Distribution of yield strength in the center of the horizontal and vertical bars due to uncertainty in material properties

4 Conclusion

In summary, we have presented a multiscale framework for uncertainty quantification and propagation of the laser powder-bed fusion (PBF-L) process. With Inconel718 as base material and process parameters set at default for EOSM290 printer, we have performed systematic study based on a bar design, printed horizontally and vertically on the build plate. Data generation and propagation began at the scale of the part, where thermal history was calculated. Then, layer temperature was applied as the boundary condition for high-fidelity melt pool simulations at the scale of the powder, which generated the grain structure in 3D. This information was then taken as the input to a mean-field homogenization scheme, which ultimately computed the stress-strain curve including yield strength. By modeling material properties (thermal conductivity, specific heat, and density) as random variables, we quantitatively showed how their uncertainty

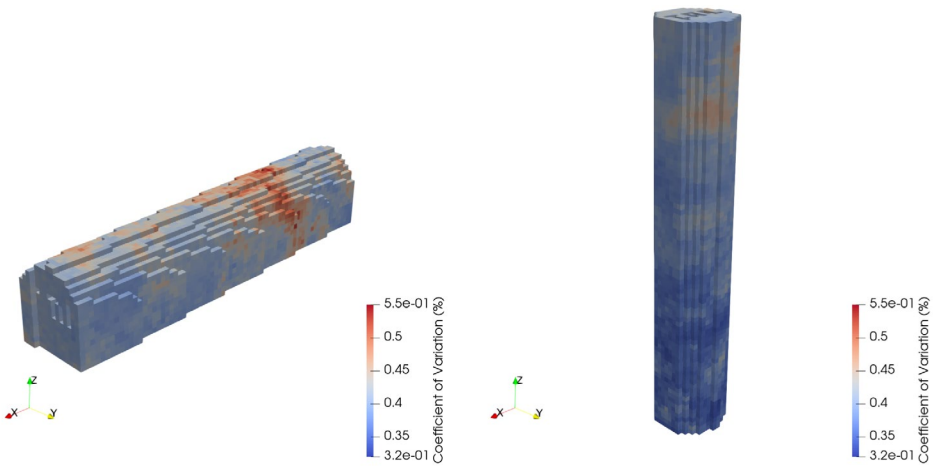

(a) Horizontal (b) Vertical

Fig. 18 Distribution of the coefficient of variation (%) in the horizontal and vertical bars

propagated into yield strength. Because of their different ability to conduct heat away into the baseplate, a horizontal and a vertical bar have different microstructure, mechanical properties, as well as uncertainty in yield strength. Our results show that uncertainty is particularly pronounced in vertical bars. Such conclusion gives insights to the manufacturing process engineer, suggesting that printing parts in close contact with the baseplate is a practical method to minimize uncertainty in the parts' mechanical properties, thus providing an additional guideline for manufacturing of high-quality parts.

This work introduces a process–thermal–structure–property framework to systematically quantify how build orientation alters thermal history, microstructure evolution, and spatial variation in yield strength during PBF-L fabrication. In addition, it establishes a multi-scale uncertainty propagation framework that links material uncertainties to part-level mechanical variability, providing a foundation for reliability assessment and digital certification of additively manufactured components. In additive manufacturing, intricated part geometries, such as lattice structures and overhangs, are often employed, which can lead to complex heat accumulation during the build process. For such complex geometries, our results suggest that a different material uncertainty at different part orientation will necessarily be present, due to the inevitably different contact points of the part with the baseplate at different build orientations. In our work, the impact of convection heat transfer coefficient as well as baseplate preheating temperature was not specifically studied. Sensitivity analysis on the results showed that such parameters have a small quantitative impact on the temperature profiles, and do not alter the conclusions of this work.

Author Contributions Umesh Kizhakkinan: Writing - Original Draft, Conceptualization, Methodology, Formal analysis, Investigation. Jakub Mikula: Software, Writing - Review & Editing. Shemuel Joash Kuehsamy: Software. Yingzhi Zeng: Software. Kewu Bai: Software. Robert Laskowski: Software, Writing - Review & Editing. Nagarajan Raghavan: Writing - Review & Editing, Supervision, Funding acquisition. Guglielmo Vastola: Writing - Review & Editing, Supervision, Project administration, Funding acquisition. Yong-Wei Zhang: Writing - Review & Editing, Supervision, Project administration, Funding acquisition. All authors read and approved the final manuscript.

Funding This research is supported by A*STAR under its Advanced Models for Additive Manufacturing (AM^2) programme (Award M22L2b0111). Any opinions, findings and conclusions or recommendations expressed in this material are those of the author(s) and do not reflect the views of the A*STAR.

Declarations

Competing Interests The authors have no relevant financial or non-financial interests to disclose.

References

1. Gibson I, Rosen D, Stucker B, Khorasani M (2021) Additive Manufacturing Technologies, 3rd edn. Springer International Publishing, Switzerland
2. Hu Z, Mahadevan S (2017) Uncertainty quantification and management in additive manufacturing: current status, needs, and opportunities. Intern J Adv Manuf Technol 93:2855–2874. https://doi.org/10.1007/S00170-017-0703-5
3. Mahadevan S, Nath P, Hu Z (2022) Uncertainty Quantification for Additive Manufacturing Process Improvement: Recent Advances. ASCE-ASME J Risk Uncertain Eng Syst Part B Mechan Eng 8(1):010801. https://doi.org/10.1115/1.4053184
4. Hu Z, Mahadevan S (2017) Uncertainty quantification in prediction of material properties during additive manufacturing. Scripta Mater 135:135–140. https://doi.org/10.1016/J.SCRIPTAMAT.2016.10.014
5. Moges T, Ameta G, Witherell P (2019) A Review of Model Inaccuracy and Parameter Uncertainty in Laser Powder Bed Fusion Models and Simulations. J Manuf Sci Eng Trans ASME 141(4). https://doi.org/10.1115/1.4042789
6. Lopez F, Witherell P, Lane B (2016) Identifying uncertainty in laser powder bed fusion additive manufacturing models. J Mechan Design Trans ASME 138(11):114502. https://doi.org/10.1115/1.4034103

7. Tapia G, King W, Johnson L, Arroyave R, Karaman I, Elwany A (2018) Uncertainty propagation analysis of computational models in laser powder bed fusion additive manufacturing using polynomial chaos expansions. J Manuf Sci Eng 140(12):121006. https://doi.org/10.1115/1.4041179
8. Moges T, Yan W, Lin S, Ameta G, Fox J, Witherell P (2018) Quantifying Uncertainty in Laser Powder Bed Fusion Additive Manufacturing Models and Simulations. In: International Solid Freeform Fabrication Symposium. University of Texas at Austin pp 1913–1928. Available from: https://doi.org/10.26153/TSW/17193
9. Wang Z, Liu P, Ji Y, Mahadevan S, Horstemeyer MF, Hu Z et al (2019) Uncertainty Quantification in Metallic Additive Manufacturing Through Physics-Informed Data-Driven Modeling. JOM 71:2625–2634. https://doi.org/10.1007/s11837-019-03555-z
10. Moser D, Cullinan M, Murthy J (2019) Multi-scale computational modeling of residual stress in selective laser melting with uncertainty quantification. Addit Manuf 29:100770. https://doi.org/10.1016/j.addma.2019.06.021
11. Ghosh S, Mahmoudi M, Johnson L, Elwany A, Arroyave R, Allaire D (2019) Uncertainty analysis of microsegregation during laser powder bed fusion. Modell Simul Mater Sci Eng 27:034002. https://doi.org/10.1088/1361-651X/ab01bf
12. Wang Z, Jiang C, Liu P, Yang W, Zhao Y, Horstemeyer MF et al (2020) Uncertainty quantification and reduction in metal additive manufacturing. NPJ Comput Mater 6:1–10. https://doi.org/10.1038/s41524-020-00444-x
13. Wells S, Plotkowski A, Krane MJM (2021) Propagation of Input Uncertainties in Numerical Simulations of Laser Powder Bed Fusion. Metall Mater Trans B 52:3016–3031. https://doi.org/10.1007/S11663-021-02218-2/TABLES/8
14. Moges T, Jones K, Feng S, Witherell P, Ameta G (2022) On Characterizing Uncertainty Sources in Laser Powder-Bed Fusion Additive Manufacturing Models. ASCE-ASME J Risk Uncertain Eng Syst Part B Mechan Eng 8(1):011110. https://doi.org/10.1115/1.4052039/1115613
15. Nath P, Sato M, Karve P, Mahadevan S (2022) Multi-fidelity Modeling for Uncertainty Quantification in Laser Powder Bed Fusion Additive Manufacturing. Integrat Mater Manuf Innov 11:256–275. https://doi.org/10.1007/S40192-022-00260-9/METRICS
16. Ranaiefar M, Honarmandi P, Ye J, Zhang C, Xue L, Elwany A et al (2023) Uncertainty quantification and propagation across a multi-model computational framework for the tailored design of additively manufactured shape memory alloys. Addit Manuf 68:103506. https://doi.org/10.1016/J.ADDMA.2023.103506
17. Wu N, Whalen B, Ma J, Balachandran PV (2024) Probabilistic Printability Maps for Laser Powder Bed Fusion Via Functional Calibration and Uncertainty Propagation. J Comput Inf Sci Eng 24. https://doi.org/10.1115/1.4063727/1169238
18. Chiappetta M, Piazzola C, Tamellini L, Reali A, Auricchio F, Carraturo M (2024) Data-informed uncertainty quantification for laser-based powder bed fusion additive manufacturing. Int J Numer Meth Eng 125(17):e7542. https://doi.org/10.1002/NME.7542
19. Thakre U, Mote RG (2022) Uncertainty quantification and statistical modeling of selective laser sintering process using polynomial chaos based response surface method. J Manuf Process 81:893–906. https://doi.org/10.1016/j.jmapro.2022.07.022
20. Pham TQD, Hoang TV, Tran XV, Fetni S, Duchêne L, Tran HS et al (2023) A framework for the robust optimization under uncertainty in additive manufacturing. J Manuf Process 103:53–63. https://doi.org/10.1016/j.jmapro.2023.08.009
21. Amirian A, Battley M, Diegel O, Amirpour M (2025) Additive manufacturing defects in polymeric lattice structures: a comprehensive analysis of morphology, distribution, and printing orientation influence. Intern J Adv Manuf Technol 140:5361–5384. https://doi.org/10.1007/s00170-025-16521-8
22. Amirian A, Battley M, Amirpour M (2025) Characterisation of process-induced defects in polymeric strut-based lattice structures produced by the powder bed fusion additive manufacturing process. Rapid Prototyp J 5(31):1656–1674. https://doi.org/10.1108/RPJ-08-2024-0352
23. Jia Y, Naceur H, Saadlaoui Y, Dubar L, Bergheau JM (2024) A comprehensive comparison of modeling strategies and simulation techniques applied in powder-based metallic additive manufacturing processes. J Manuf Process 110:1–29. https://doi.org/10.1016/j.jmapro.2023.12.048
24. Bai R, Shi S, Wang J, Luo J, Pu H, Lyu W et al (2024) Investigation of printing turn angle effects on structural deformation and stress in selective laser melting. Mater Design 247:113347. https://doi.org/10.1016/j.matdes.2024.113347
25. Bai R, Shi S, Chen C, Ren Y, Yuan J, Lyu W et al (2025) Printing path optimization in selective laser melting: Deep reinforcement learning with an enhanced reward function. J Manuf Process 155:760–774. https://doi.org/10.1016/j.jmapro.2025.10.042
26. Mikula J, Laskowski R, Dai L, Ding W, Wei M, Bai K et al (2021) Advanced "Digital Twin" platform for powder-bed fusion additive manufacturing. Proterial Technical Reports. Available from: https://www.proterial.com/rad/paper/technical_report/pdf/vol37_r01.pdf
27. Wei M, Ding WJ, Vastola G, Zhang YW (2022) Quantitative study on the dynamics of melt pool and keyhole and their controlling factors in metal laser melting. Addit Manuf 54:102779. https://doi.org/10.1016/j.addma.2022.102779
28. Laskowski R, Ahluwalia R, Hock GTW, Ying CS, Sun CN, Wang P et al (2022) Concurrent modeling of porosity and microstructure in multilayer three-dimensional simulations of powder-bed fusion additive manufacturing of INCONEL 718. Addit Manuf 60:103266. https://doi.org/10.1016/j.addma.2022.103266
29. Ghorbanpour S, Zecevic M, Kumar A, Jahedi M, Bicknell J, Jorgensen L et al (2017) A crystal plasticity model incorporating the effects of precipitates in superalloys: Application to tensile, compressive, and cyclic deformation of Inconel 718. Int J Plast 99:162–185. https://doi.org/10.1016/j.ijplas.2017.09.006
30. Agazhanov AS, Samoshkin DA, Kozlovskii YM (2019) Thermophysical properties of Inconel 718 alloy. J Phys: Conf Ser 1382(1):012175. https://doi.org/10.1088/1742-6596/1382/1/012175
31. Moelans N, Blanpain B, Wollants P (2008) Quantitative analysis of grain boundary properties in a generalized phase field model for grain growth in anisotropic systems. Phys Rev B 78:024113. https://doi.org/10.1103/PhysRevB.78.024113
32. Heulens J, Blanpain B, Moelans N (2011) A phase field model for isothermal crystallization of oxide melts. Acta Mater 59(5):2156–2165. https://doi.org/10.1016/j.actamat.2010.12.016
33. Chatterjee S, Moelans N (2021) A grand-potential based phase-field approach for simulating growth of intermetallic phases in multicomponent alloy systems. Acta Mater 206:116630. https://doi.org/10.1016/j.actamat.2021.116630
34. Steinbach I (2009) Phase-field models in materials science. Modell Simul Mater Sci Eng 17(7):073001. https://doi.org/10.1088/0965-0393/17/7/073001
35. Radhakrishnan B, Gorti SB, Turner JA, Acharya R, Sharon JA, Staroselsky A et al (2019) Phase Field Simulations of Microstructure Evolution in IN718 Using a Surrogate Ni-Fe-Nb Alloy during Laser Powder Bed Fusion. Metals 9(1). https://doi.org/10.3390/met9010014
36. Gandin CA, Rappaz M, Tintillier R (1994) 3-Dimensional simulation of the grain formation in investment castings. Metall and Mater Trans A 25(3):629–635. https://doi.org/10.1007/BF02651604
37. Dong HB, Lee PD (2005) Simulation of the columnar-to-equiaxed transition in directionally solidified Al-Cu alloys. Acta Mater 53(3):659–668. https://doi.org/10.1016/j.actamat.2004.10.019

38. Shao J, Yu G, He X, Li S, Chen R, Zhao Y (2019) Grain size evolution under different cooling rate in laser additive manufacturing of superalloy. Optics Laser Technol 119:105662. https://doi.org/10.1016/j.optlastec.2019.105662
39. Kavousi S, Gates A, Jin L, Asle ZM (2022) A temperature-dependent atomistic-informed phase-field model to study dendritic growth. J Cryst Growth 579:126461. https://doi.org/10.1016/j.jcrysgro.2021.126461
40. Hutchinson JW, Hill R (1970) Elastic-plastic behaviour of polycrystalline metals and composites. Proceed Royal Soc London A Math Phys Sci 319(1537):247–272. https://doi.org/10.1098/rspa.1970.0177
41. The MathWorks Inc.: MATLAB version: 24.02 (R2024a). Natick, Massachusetts, United States: The MathWorks Inc., Available from: https://www.mathworks.com
42. Promoppatum P, Yao SC, Pistorius PC, Rollett AD, Coutts PJ, Lia F et al (2018) Numerical modeling and experimental validation of thermal history and microstructure for additive manufacturing of an Inconel 718 product. Progress Addit Manuf 3:15–32. https://doi.org/10.1007/s40964-018-0039-1
43. Sweet JN, Roth EP, Moss M (1987) Thermal conductivity of Inconel 718 and 304 stainless steel. Int J Thermophys 8:593–606. https://doi.org/10.1007/BF00503645
44. Yang Y, Wang P, Brandenberg SJ (2022) An algorithm for generating spatially correlated random fields using Cholesky decomposition and ordinary kriging. Comput Geotech 147:104783. https://doi.org/10.1016/j.compgeo.2022.104783
45. Kizhakkinan U, Rosen DW, Raghavan N (2024) Uncertainty propagation in fused filament fabrication process: a multiscale approach. Intern J Adv Manuf Technol 135:281–300. https://doi.org/10.1007/s00170-024-14464-0